Electric 3D-Simulation of Metallized Film Capacitors

J. Ostrowski[1], R. Hiptmair and H. Fuhrmann[2]

---

[1] ABB Switzerland Ltd., e-mail: joerg.ostrowski@ch.abb.com
[2] ABB Switzerland Ltd., e-mail: henning.fuhrmann@ch.abb.com

Electric 3D-Simulation of Metallized Film Capacitors

J. Ostrowski[1], R. Hiptmair and H. Fuhrmann[2]

Seminar für Angewandte Mathematik
Eidgenössische Technische Hochschule
CH-8092 Zürich
Switzerland

Abstract

Purpose - This paper deals with the computation of time-harmonic electric potentials, currents, and surface charge distributions inside self-healing metallized film capacitors in three dimensions. A 50 Hz exciting voltage is applied at contacts.

Design/methodology/approach - Extreme aspect ratios warrant dimensional reduction: the metallization is modelled as a two-dimensional shell. This greatly reduces computational costs and makes possible an excellent resolution of the geometry. An integro-differential equation for the complex amplitudes of the electric potential and surface charge densities on this shell is derived and discretized by means of boundary elements (BEM).

Findings - Adaptive cross approximation (ACA) and $\mathcal{H}$-matrix technology is employed for matrix compression and preconditioning of iterative solvers. This permits us to use fine surface meshes and achieve satisfactory accuracy as demonstrated in numerical experiments.

Research limitations/implications - The model is based on an electroquasistatic approach, thus it is valid for low frequencies only.

Practical implications - Numerical experiments of sophisticated real-life capacitor-designs show the efficacy of the method for industrial applications.

Originality/value - We developed and implemented a novel model for the three-dimensional electric field computation inside metallized film capacitors in the frequency domain.

Keywords: Film capacitors, electric field computation, extreme aspect ratios, dimensional reduction, boundary element method, $\mathcal{H}$-matrices

---

[1] ABB Switzerland Ltd., e-mail: joerg.ostrowski@ch.abb.com
[2] ABB Switzerland Ltd., e-mail: henning.fuhrmann@ch.abb.com

1   Self-Healing Metallized Film Capacitors

Phase-shifts caused by inductivities lead to unwanted losses and disturbances in electrical networks. Capacitive elements reduce these network losses, stabilize the network voltage and increase the power factor. *Self-healing metallized film capacitors* (Berqvist, Törnkvist and Mood 2004, Drugge, Carlen, Laihonen and Spronck 2003) can be used for that purpose and have first been examined in the fifties by (Charlton 1955, Kohler 1956, Sträb 1954). Self-healing metallized film capacitors consist of a very thin polymer film with a thickness, t_D, of 5 to 20 μm and a width, w_D, of several centimeters. Polymer films have high electric strength, i.e., they maintain insulation even in the presence of very large electric fields. Conducting layers of metal (typically Al or Zn) are vacuum-deposited onto the surface of the film. This so-called metallization has a thickness, δ, of only 5 to 100 nm. The advantage of metallized film capacitors is that they are *self-healing* or *clearing* with respect to small defects, which are always present in industrially produced dielectric films (Christen and Carlen 2003, Heywang 1976, Kammermaier 1964, Kammermaier, Rittmayer and Birkle 1989, Reed and Cichanowski 1994). When an electrical breakdown occurs at the small defect, the metallization evaporates and effectively insulates the defect from the rest of the capacitor. This limits the damage to the loss of only a few square millimeters of capacitive area.
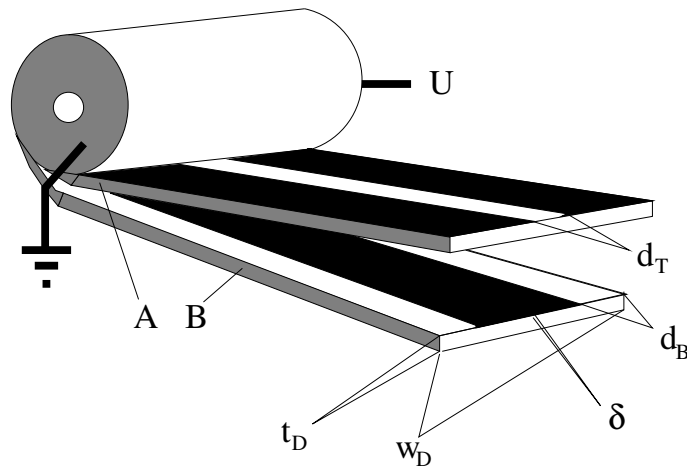

Figure 1: Sketch of a metallized film capacitor with two sheets, Sheet A and Sheet B. Dielectric film thickness $t_D = 6\mu$m, dielectric film width $w_D = 55$mm, metallization thickness $\delta = 20$nm, axial track distance $d_T = 5$mm, Sheet B track-contact distance $d_B = 2.5$mm. Conductive contact material is depicted in grey, metallization in black and dielectric film in white.

Depending on the application, various different metallization patterns are in use. In this article we will examine the configuration shown in Figure 1. The capacitor is manufactured by winding several turns of two different sheets (Sheet A and Sheet B) of metallized film onto a cylindrical core. The resulting capacitor has the shape of a cylindrical roll. A sprayed-on layer of conductive contact material connects the metallized tracks of Sheet A to the voltage supply on each end of the cylindrical roll, whereas the metallization of Sheet B is floating. Electrically, this is equivalent to a serial connection of two capacitors.

Such a capacitor can be further optimized by adding a segment structure to the metallization pattern (Carlen and Brüesch 1996), see Figure 2. These structures offer, on the one hand, additional safety since the incorporated fuses will disconnect a failing segment in the case of large breakdown currents. On the other hand, the disconnected segment is left floating, capacitively coupled to the rest of the winding in an inherently three-dimensional way. This could lead to overvoltages or additional loss currents in the vicinity of the failed segment. Unfortunately this situation can neither be investigated experimentally nor by simple models with analytic solutions. Thus, numerical simulation must play a key role in optimizing the design of the metallization. However,
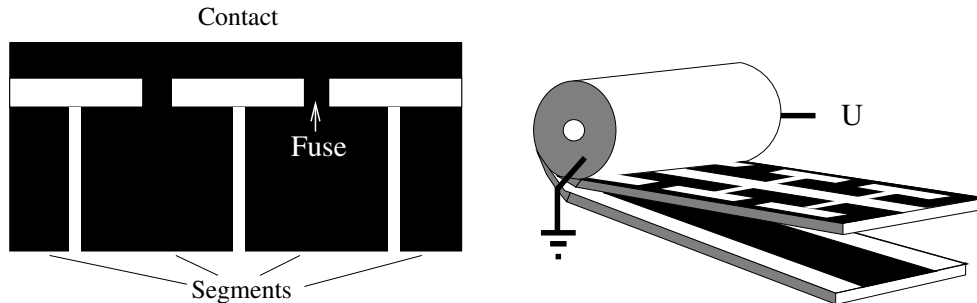
Figure 2: Optimized design based on a segment structure with fuses.

no effective simulation approaches have been available until now.

In this paper we propose an appropriate numerical method for the computation of electric fields inside self-healing metallized film capacitors. We face extreme aspect ratios in non-symmetric and three-dimensional configurations, as can be seen in Figures 1 and 2. The huge aspect ratios, $w_D : t_D$ and $w_D : \delta$, pose the main challenge. The sheer size of these aspect ratios compounds the difficulties of creating a spatial finite element mesh. The main obstacle is that the thickness, δ, of the metallization is in the range of a few nanometers. However, we do not expect any significant variation of the field across this very thin metallization. Hence, we can safely ignore such a variation and carry out dimensional reduction: the metal layer will be represented by a two-dimensional surface.

This simplification is only a partial remedy, since we still have to cope with the thickness, t_D, of the film in the range of micrometers, which is quite small compared to its width, w_D. Fortunately, the interior of the dielectric film can be treated with a boundary integral method, which does not require the meshing of the volume. Thus, we merely need a two-dimensional triangulation of the metallization for the whole simulation. The bad aspect ratio that originates from the film thickness is automatically and properly removed by the usage of a *boundary element method* (BEM).

Of course we cannot compute the total length of the film that is wound on the roll, because this amounts to several meters. As an approximation, we assume that the field on any one turn of the capacitor is mainly produced by charges on the turns in the close neighborhood, and that the turns further away can be neglected. This can also be justified by the fact that all electrically induced charges will locally try to equalize the exciting charges, which means that long range monopole terms vanish. Thus we only model a couple of turns instead of the complete capacitor.

In the next section we start from an *electroquasistatic model*, conduct and justify dimensional reduction and derive the relevant equations. In Section 3 we give a variational formulation and prove its well-posedness. In Section 4 we present the boundary element Galerkin discretization and discuss issues of matrix compression and preconditioning. Finally, we report in Section 5 on the performance of the method for several test problems.

2   Electroquasistatic modelling

The regime of the electrodynamic phenomena underlying the behavior of the capacitor is marked by

- an excitation at moderate frequencies, at which electromagnetic wavelengths are much larger than the size of the capacitor,

- the dominance of electric field energy (capacitive effects) compared to magnetic field energy (inductive effects).

2

This justifies the use of the *electroquasistatic* approximation of Maxwell's equations (Dirks 1996, Kiang 1996, Reitzinger, Schreiber and van Rienen 2003), which formally amounts to setting the magnetic induction to zero in Maxwell's equations. This involves $\mathbf{curl}\,\mathbf{E} = 0$ and permits us to express the electric field as the gradient of a scalar potential $\mathbf{E} = -\mathbf{grad}\,\phi$. Ampère's law is retained, so that the full electroquasistatic model reads

$$\mathbf{E} = -\mathbf{grad}\,\phi \quad , \quad \mathbf{curl}\,\mathbf{H} = \tfrac{\partial}{\partial t}(\epsilon \mathbf{E}) + \mathbf{j} \,. \tag{1}$$

Next, we assume linear materials and that Ohm's law $\mathbf{j} = \sigma \mathbf{E}$ holds inside the conducting film. Thus, in view of the time-harmonic voltage excitation with fixed angular frequency ω, the governing equations (1) can be transformed in the frequency domain:

$$\mathbf{E} = -\mathbf{grad}\,\phi \quad , \quad \mathbf{curl}\,\mathbf{H} = i\omega\epsilon\mathbf{E} + \sigma\mathbf{E} \,. \tag{2}$$

Taking the divergence of the second equation yields the final equation for the (complex) phasor of the scalar potential,

$$-\operatorname{div}\left(\epsilon + {}^{\sigma}/_{i\omega}\right)\mathbf{grad}\,\phi = 0 \,, \tag{3}$$

which generically holds in all of $\mathbb{R}^3$. The contacts are taken into account by fixing the potential on certain parts Γ_c of the surface of the conductors.

We now consider (3) separately in the part Ω_C of space occupied by the conductors (the metallization) and in the remaining insulating dielectric region $\Omega_D := \mathbb{R}^3 \setminus \Omega_C$ (the polymer film). Integrating (3) over Ω_C against a test function ϕ' that vanishes on the contact zones Γ_c, and performing integration by parts, we obtain

$$\int_{\Omega_C} \left(\epsilon + {}^{\sigma}/_{i\omega}\right)\mathbf{grad}\,\phi_C \cdot \mathbf{grad}\,\phi'\,\mathrm{d}\mathbf{r} = \int_{\partial\Omega_C \setminus \Gamma_c} g_C\,\phi'\,\mathrm{d}S \,, \tag{4}$$

where we wrote $g_C := \left(\epsilon + {}^{\sigma}/_{i\omega}\right)\mathbf{grad}\,\phi_C \cdot \mathbf{n}$, $\mathbf{n}$ standing for the exterior unit normal vectorfield on the surface $\partial\Omega_C$ of the conducting region[1].

In the nonconducting dielectric region, the dielectric tensor ϵ is assumed to be constant with value ϵ_D, so that we encounter a harmonic potential ϕ_D there, which allows a representation by boundary potentials (Sauter and Schwab 2004, Thm. 3.1.6)

$$\phi_D(\mathbf{r}) = \int_{\partial\Omega_C} \frac{1}{4\pi\epsilon_D|\mathbf{r}-\mathbf{r}'|} g_D(\mathbf{r}')\,\mathrm{d}S(\mathbf{r}') + \int_{\partial\Omega_C} \frac{(\mathbf{r}-\mathbf{r}')\cdot\mathbf{n}(\mathbf{r}')}{4\pi\epsilon_D|\mathbf{r}-\mathbf{r}'|^3}\phi_D(\mathbf{r}')\,\mathrm{d}S(\mathbf{r}') \quad , \quad \mathbf{r} \in \Omega_D \quad , \tag{5}$$

where $g_D := -\epsilon_D\,\mathbf{grad}\,\phi_D \cdot \mathbf{n}$ is the electric displacement flux density through $\partial\Omega_C$. The equations (4) and (5) are connected by the *transmission conditions* implied by the tangential continuity of both $\mathbf{E}$ and $\mathbf{H}$:

$$\phi_C = \phi_D \quad \text{and} \quad g_C = g_D \quad \text{on } \partial\Omega_C \,. \tag{6}$$

This permits us to refer to a unique quantity $g := g_C = g_D$ on $\partial\Omega_C$. We remark that the transmission conditions in conjunction with (4) and (5), give rise to a coupling of a variational formulation inside Ω_C and of a boundary integral formulation in Ω_D (Johnson and Nédélec 1980, Costabel 1987).

Yet, we aim to exploit the extreme aspect ratios present in the capacitor setting in order to carry out *dimensional reduction* and arrive at a much simpler coupled formulation.

To begin with, the conducting film occupying Ω_C is supposed to have uniform thickness, δ, so that

$$\Omega_C := \left\{ \mathbf{r} = (\mathbf{x} + \xi\mathbf{d}(\mathbf{x})) \in \mathbb{R}^3 : \mathbf{x} \in \Sigma, -\tfrac{\delta}{2} < \xi < \tfrac{\delta}{2} \right\} \,, \tag{7}$$

---

[1] Here and below, the subscript C tags functions on Ω_C. Quantities belonging to Ω_D will bear a subscript D
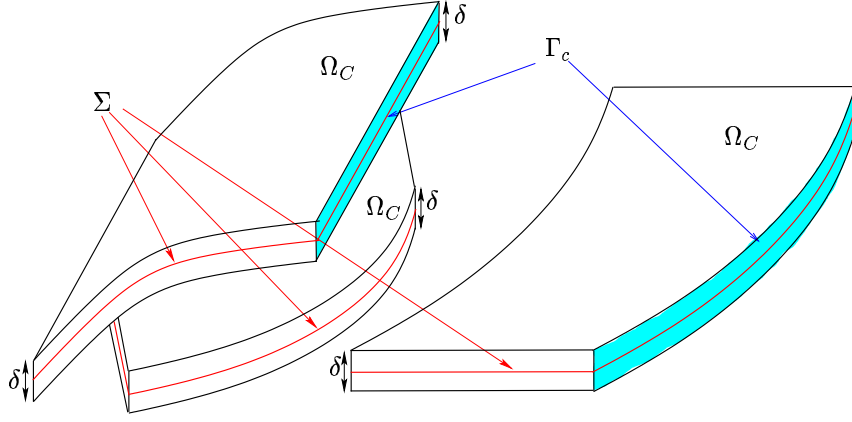
Figure 3: Skeleton surface for thin sheets

where the "skeleton" Σ is a smooth bounded surface with transversal normal direction $\mathbf{d}$, see Figure 3. The thickness δ has to be small enough to render (7) a valid parameterization of Ω_C.

Next, we neglect any transversal variation of the potential inside the conducting film:

$$\phi_C(\mathbf{x} + \xi \mathbf{d}(\mathbf{x})) = \phi(\mathbf{x}) , \quad \mathbf{x} \in \Sigma , \quad -\tfrac{\delta}{2} < \xi < \tfrac{\delta}{2} . \tag{8}$$

For a thin conducting film this is a reasonable assumption, because a significant transversal drop in the potential would amount to extremely strong electric fields, which would immediately be offset by an accumulation of surface charges. In addition, we do not admit any transversal variation of conductivity and dielectric constant inside Ω_C. Also the applied potential at the contacts must be constant in thickness direction.

Another simplification consists in ignoring fields emanating from the edges of the thin film. This is justified by their very small contribution to the total surface $\partial\Omega_C$. Fields that originate from the edge are only relevant in the vicinity of the edge, for distances of similar size as the edge-radius ($\approx \delta/2$). Thus field enhancements around the edge can neither be computed by our model, nor need to be taken into account for the purpose of this study.

Once we have made these assumptions, (4) can be equivalently written as

$$\delta \int_\Sigma \left(\epsilon(\mathbf{x}) + {}^{\sigma(\mathbf{x})}/_{i\omega}\right) \mathbf{grad}_\Sigma \, \phi(\mathbf{x}) \cdot \mathbf{grad}_\Sigma \, \phi'(\mathbf{x}) \, \mathrm{d}S(\mathbf{x}) = \int_\Sigma q(\mathbf{x}) \, \phi'(\mathbf{x}) \, \mathrm{d}S(\mathbf{x}) \quad \forall \phi' , \tag{9}$$

where $\mathbf{grad}_\Sigma$ stands for the surface gradient on Σ, and

$$q(\mathbf{x}) := g_C(\mathbf{x} + \tfrac{\delta}{2}\mathbf{d}(\mathbf{x})) + g_C(\mathbf{x} - \tfrac{\delta}{2}\mathbf{d}(\mathbf{x})) . \tag{10}$$

Also in the boundary potential representation formula we are going to ignore the contribution of edge parts of $\partial\Omega_C$ and the local curvature of Σ, so that (5) becomes

$$\phi_D(\mathbf{r}) \approx \int_\Sigma \frac{1}{4\pi\epsilon_D|\mathbf{r} - (\mathbf{x} + \tfrac{\delta}{2}\mathbf{d})|} g_D(\mathbf{x} + \tfrac{\delta}{2}\mathbf{d}) + \frac{1}{4\pi\epsilon_D|\mathbf{r} - (\mathbf{x} - \tfrac{\delta}{2}\mathbf{d})|} g_D(\mathbf{x} - \tfrac{\delta}{2}\mathbf{d}) \, \mathrm{d}S(\mathbf{x}) +$$

$$\int_\Sigma \frac{(\mathbf{r} - (\mathbf{x} + \tfrac{\delta}{2}\mathbf{d})) \cdot \mathbf{d}(\mathbf{x})}{4\pi\epsilon_D|\mathbf{r} - (\mathbf{x} + \tfrac{\delta}{2}\mathbf{d})|^3} \, \phi_D(\mathbf{x} + \tfrac{\delta}{2}\mathbf{d}) - \frac{(\mathbf{r} - (\mathbf{x} - \tfrac{\delta}{2}\mathbf{d})) \cdot \mathbf{d}(\mathbf{x})}{4\pi\epsilon_D|\mathbf{r} - (\mathbf{x} - \tfrac{\delta}{2}\mathbf{d})|^3} \, \phi_D(\mathbf{x} - \tfrac{\delta}{2}\mathbf{d}) \, \mathrm{d}S(\mathbf{x}) , \quad (11)$$

because the exterior unit normals have opposite directions on both sides of $\partial\Omega_C$. Next, we use the first order approximation $\mathbf{r} - (\mathbf{x} \pm \tfrac{\delta}{2}\mathbf{d}) \approx \mathbf{r} - \mathbf{x}$, taking into account the transmission condition

4

(6) and that ϕ_C does not vary in transversal direction. This will make the second integral of (11) vanish, which means

$$\phi_D(\mathbf{r}) \approx \int\limits_\Sigma \frac{1}{4\pi\epsilon_D|\mathbf{r}-\mathbf{x}|}\,q(\mathbf{x})\,\mathrm{d}S(\mathbf{x})\,, \quad \mathbf{r}\in\Omega_D\,. \tag{12}$$

We can identify (12) as single layer representation of the potential created by a sheet with area charge density q. We conclude this from the fact that the electric displacement $-\epsilon_D\,\mathbf{grad}\,\phi_D$ has a jump of size q across Σ.

For the single layer potential (12) the trace on Σ is well defined, so that we can admit $\mathbf{r}\in\Sigma$. Subsequently, we cast the resulting equation in weak form and use the other transmission condition $\phi_D = \phi_C$ on Σ

$$\int\limits_\Sigma \phi(\mathbf{x})\cdot q'(\mathbf{x})\,\mathrm{d}S(\mathbf{x}) = \int\limits_\Sigma\int\limits_\Sigma \frac{1}{4\pi\epsilon_D|\mathbf{x}-\mathbf{x}'|}\,q(\mathbf{x})q'(\mathbf{x}')\,\mathrm{d}S(\mathbf{x}')\mathrm{d}S(\mathbf{x}) \quad \forall q'\,. \tag{13}$$

The two variational equations (9) and (13) for the unknown film potential ϕ and charge density q immediately lend themselves to coupling.

3 Theory

Before we state the final coupled variational equations, we have to fit the equations into a proper framework of function spaces on Σ. First equation (9) requires trial and test functions to possess a square integrable surface gradient. Further, the test functions are supposed to vanish on the contacts, which suggests the test space

$$H^1_{\Gamma_c}(\Sigma) := \{v\in H^1(\Sigma) : v = 0 \text{ on } \Gamma_c\}\,. \tag{14}$$

As we integrate the surface charge density, q, against a function from $H^1_{\Gamma_c}(\Sigma)$ it has to belong to the dual space of $H^1_{\Gamma_c}(\Sigma)$.

We derived (12) by taking a trace on Σ, which means that (12) has to be read as an equation in the trace space $H^{\frac{1}{2}}(\Sigma)$, so that the proper test space in (13) is the dual space $\widetilde{H}^{-\frac{1}{2}}(\Sigma)$ (Sauter and Schwab 2004, Section 3.5.3). Also recall that the operator induced by the weak interpretation of the single layer boundary integral operator, $cf.$ (13), provides a continuous mapping $\widetilde{H}^{-\frac{1}{2}}(\Sigma) \mapsto H^{\frac{1}{2}}(\Sigma)$ (Sauter and Schwab 2004, Thm. 3.1.16). This suggests that we actually seek q in the space $\widetilde{H}^{-\frac{1}{2}}(\Sigma)$. Summing up, we arrive at the following coupled problem:

Find the surface charge density $q\in\widetilde{H}^{-\frac{1}{2}}(\Sigma)$ and the potential $\phi\in H^1(\Sigma)$, $\phi_{|\Gamma_c} = u$, such that

$$\int\limits_\Sigma\int\limits_\Sigma \frac{q(\mathbf{x}')q'(\mathbf{x})}{4\pi\epsilon_D|\mathbf{x}-\mathbf{x}'|}\,\mathrm{d}S(\mathbf{x}')\mathrm{d}S(\mathbf{x}) - \int\limits_\Sigma \phi(\mathbf{x})\,q'(\mathbf{x})\,\mathrm{d}S(\mathbf{x}) = 0 \quad \forall q'\in\widetilde{H}^{-\frac{1}{2}}(\Sigma)\,, \tag{15}$$

$$\int\limits_\Sigma q(\mathbf{x})\,\phi'(\mathbf{x})\,\mathrm{d}S(\mathbf{x}) + \delta\int\limits_\Sigma (\epsilon + {}^{\sigma}/i\omega)\,\mathbf{grad}_\Sigma\,\phi\cdot\mathbf{grad}_\Sigma\,\phi'\,\mathrm{d}S(\mathbf{x}) = 0 \quad \forall\phi'\in H^1_{\Gamma_c}(\Sigma)\,. \tag{16}$$

Here, $u\in H^{\frac{1}{2}}(\Gamma_c)$ models the externally applied voltage at the contact edges.

Theorem 1 *The variational problem* (16), (15) *is well posed.*

5

Proof. Let us denote by $\Sigma_1, \ldots, \Sigma_m$ the connected components of Σ. For the sake of simplicity we assume that only one of them, say Σ_1, does not possess a contact. We split

$$H_{\Gamma_c}^1(\Sigma) = \{\psi \in \mathcal{H}_{\Gamma_c}^1(\Sigma) : \int_{\Sigma_1} \psi \, \mathrm{d}S = 0\} \oplus \mathbb{C} =: H_*^1(\Sigma) \oplus \mathbb{C} \ . \tag{17}$$

Plugging the corresponding decomposition of $\phi = \overline{\phi} + c$ and $\phi' = \overline{\phi}' + c'$ into (16), (15) we end up with: seek $\phi \in H_*^1(\Sigma)$, $\phi_{|\Gamma_c} = u$, $c \in \mathbb{C}$, and $q \in \widetilde{H}^{-\frac{1}{2}}(\Sigma)$ such that

$$\begin{array}{cccccl}
\iint_{\Sigma \Sigma} \frac{q(\mathbf{x}')q'(\mathbf{x})}{4\pi\epsilon_D|\mathbf{x}-\mathbf{x}'|} \, \mathrm{d}S(\mathbf{x}')\mathrm{d}S(\mathbf{x}) & - & \int_{\Sigma} \overline{\phi}\, q' \, \mathrm{d}S & + & c \int_{\Sigma_1} q'(\mathbf{x}) \, \mathrm{d}S & = \ \ldots \, , \\
\int_{\Sigma} q \, \overline{\phi}' \, \mathrm{d}S & + & \delta \int_{\Sigma} (\epsilon + \sigma/i\omega) \, \mathbf{grad}_{\Sigma}\, \overline{\phi} \cdot \mathbf{grad}_{\Sigma}\, \overline{\phi}' \, \mathrm{d}S & & & = \ \ldots \, , \\
\int_{\Sigma_1} q(\mathbf{x}) \, \mathrm{d}S & & & & & = \ 0 \, ,
\end{array} \tag{18}$$

for all $\phi' \in H_*^1(\Sigma)$, $q' \in \widetilde{H}^{-\frac{1}{2}}(\Sigma)$.

The upper left 2×2-block of this variational problem, which we abbreviate as $c((\phi,q),(\phi',q'))$, has a convenient block skew-symmetric structure:

$$\begin{aligned}
c\left(\begin{pmatrix} \overline{\phi} \\ q \end{pmatrix}, \begin{pmatrix} \overline{\phi}' \\ q' \end{pmatrix}\right) = \ & \delta \int_{\Sigma} (\epsilon + \sigma/i\omega) \, \mathbf{grad}_{\Sigma}\, \overline{\phi} \cdot \mathbf{grad}_{\Sigma}\, \overline{\phi}' \, \mathrm{d}S + \int_{\Sigma} q \, \overline{\phi}' \, \mathrm{d}S \\
& - \int_{\Sigma} \overline{\phi}\, q' \, \mathrm{d}S + \iint_{\Sigma \Sigma} \frac{q(\mathbf{x}')q'(\mathbf{x})}{4\pi\epsilon_D|\mathbf{x}-\mathbf{x}'|} \, \mathrm{d}S(\mathbf{x}')\mathrm{d}S(\mathbf{x}) \, .
\end{aligned}$$

This enables us to apply the following trick: pick any $\phi \in H_{\Gamma_c}^1$ and $q \in^{-\frac{1}{2}} (\Sigma)$. Test (16) with $\phi' := \phi^*$ and (15) with $q' := q^*$. After adding the resulting equations, the real parts of the non-positive terms cancel and we find that the bilinear form c is $H_*^1(\Sigma) \times H^{-\frac{1}{2}}(\Sigma)$-elliptic:

$$|c((\phi,q),(\phi^*,q^*))| \geq C \left\{ \delta \|\phi\|_{H^1(\Sigma)}^2 + \|q\|_{H^{-\frac{1}{2}}(\Sigma)}^2 \right\} \, ,$$

with $C > 0$ independent of ϕ and q. Here we appealed to the $H^{-\frac{1}{2}}(\Sigma)$-ellipticity of the single layer boundary integral operator (Sauter and Schwab 2004, Thm. 3.5.3).

Hence we can apply the abstract theory for variational saddle point problems (Brezzi and Fortin 1991, Ch. 2) to (18). Since $q' \mapsto \int_{\Sigma} q' \, \mathrm{d}S$ is a non-trivial functional on $\widetilde{H}^{-\frac{1}{2}}(\Sigma)$, the general theory confirms existence and uniqueness of solutions of (18) for any right hand side. $\square$

We note the following further properties of the mathematical model:

1. The mean electric current flowing tangential to metallization can be obtained from $\mathbf{j} = \sigma \, \mathbf{grad}_{\Sigma}\, \phi$.

2. If $\Sigma' \subset \Sigma$ is a connected component of Σ without contacts, then we can test (16) with $\phi' \equiv 1$ on Σ' and $\phi' \equiv 0$ elsewhere. This yields $\int_{\Sigma'} q \, \mathrm{d}S = 0$ and demonstrates that the total charge of the floating part of the metallization associated with skeleton Σ' is zero.

3. For $\omega \to 0$ the solution of (16) and (15) converges to the following limit problem:

   - the potential, ϕ, drives stationary tangential currents in the metal layer,
   - the charge density, q, becomes the unknown in a boundary integral formulation for the exterior Dirichlet problem for $-\epsilon_D \Delta \phi = 0$ in $\mathbb{R}^3 \setminus \Sigma$.

4. The system is singular for $\delta = 0$, since then we come across a boundary value problem with the potential prescribed on one-dimensional curves, which is not a valid boundary condition in 3D.

6

5. For $\sigma = 0$ we recover a valid coupled variational/boundary integral formulation for the equation $-\operatorname{div}(\epsilon\,\mathbf{grad}\,\phi) = 0$ with the potentials fixed at contacts. However, control on ϕ inside the film may be very weak for $\delta \ll 1$.

Summing up, we found the expected physical properties and models in all examined cases. The model will suffer poor conditioning for very small values of both $\delta\epsilon$ and $\delta\sigma/\omega$. We do not encounter this situation in the targeted application, because the metal layer has to be a sufficiently good conductor. Very low frequencies do not affect the model.

4   Implementation

4.1   Discretization

We equip the skeleton Σ with a piecewise flat triangulation $\mathcal{M}_h$, whose triangles define the approximate surface Σ_h. On Σ_h we introduce the boundary element space V_h of globally continuous $\mathcal{M}_h$-piecewise affine linear functions. The conforming Galerkin boundary element discretization of (15) and (16) is based on the trial and test spaces

- $V_h \subset \widetilde{H}^{-\frac{1}{2}}(\Sigma)$ for the test function q',

- $V_{h,0} := \{\psi_h \in V_h : \psi_h = 0 \text{ on } \Gamma_c\} \subset H^1_{\Gamma_c}(\Sigma)$ for test function ϕ'.

We choose the standard nodal basis of V_h comprising locally supported functions b_p, $p \in \mathcal{V}(\mathcal{M}_h)$, associated with the vertices of $\mathcal{M}_h$ (the set $\mathcal{V}(\mathcal{M}_h)$). The subset $\{b_p : p \in \mathcal{V}(\mathcal{M}_h), p \notin \overline{\Gamma}_c\}$ is used as a basis for $V_{h,0}$. Imposing an ordering of $\mathcal{V}(\mathcal{M}_h)$, we may number the basis functions $b_1, \ldots, b_N$, $N := \sharp\mathcal{V}(\mathcal{M}_h)$. We adopt the convention that $b_1, \ldots, b_L$, $L < N$, are the basis functions belonging to vertices away from the contact $\overline{\Gamma}_c$. Thus we arrive at a linear system of equations

$$\begin{bmatrix} \boldsymbol{V} & \boldsymbol{K} \\ \boldsymbol{K}^T & \boldsymbol{D} \end{bmatrix} \begin{bmatrix} \boldsymbol{q} \\ \boldsymbol{\phi} \end{bmatrix} = \begin{bmatrix} \boldsymbol{\varphi} \\ \boldsymbol{\psi} \end{bmatrix} \,, \tag{19}$$

with the dense, symmetric and positive definite matrix $\boldsymbol{V}$ that originates from the single layer boundary integral operator and two sparse matrices $\boldsymbol{K}$ and $\boldsymbol{D}$. More precisely, we find for the matrix entries

$$\boldsymbol{V}_{jl} := \int_\Sigma \int_\Sigma \frac{1}{4\pi\epsilon_D} \frac{b_j(\mathbf{x}')b_l(\mathbf{x})}{|\mathbf{x} - \mathbf{x}'|}\,\mathrm{d}S(\mathbf{x}')\,\mathrm{d}S(\mathbf{x}) \,, \qquad\qquad i,j = 1, \ldots, N \,,$$

$$\boldsymbol{K}_{jn} := -\int_\Sigma b_n(\mathbf{x}) \cdot b_j(\mathbf{x})\,\mathrm{d}S(\mathbf{x}) \,, \qquad\qquad j = 1, \ldots, N, \; n = 1, \ldots, L \,,$$

$$\boldsymbol{D}_{mn} := -\delta \int_\Sigma (\epsilon - \frac{i\sigma}{\omega})\,\mathbf{grad}_\Sigma\, b_m(\mathbf{x}) \cdot \mathbf{grad}_\Sigma\, b_n(\mathbf{x})\,\mathrm{d}S(\mathbf{x}) \,, \quad m,n = 1, \ldots, L \,.$$

The right hand side vector in (19) takes into account the excitation: writing u_k, $k = L+1, \ldots, N$, for the value of the applied voltage at the vertex $\#k$ on Γ_c, we get

$$\varphi_j := \sum_{k=L+1}^{N} u_k \int_\Sigma b_k(\mathbf{x}) \cdot b_j(\mathbf{x})\,\mathrm{d}S(\mathbf{x}) \,, \qquad\qquad j = 1, \ldots, N \,,$$

$$\psi_j := -\delta \sum_{k=L+1}^{N} u_k \int_\Sigma (\epsilon - \frac{i\sigma}{\omega})\,\mathbf{grad}_\Sigma\, b_k(\mathbf{x}) \cdot \mathbf{grad}_\Sigma\, b_j(\mathbf{x})\,\mathrm{d}S(\mathbf{x}) \,, \quad j = 1, \ldots, L \,.$$

Having solved for the unknown vectors $\boldsymbol{q} \in \mathbb{C}^N$ and $\boldsymbol{\phi} \in \mathbb{C}^L$, we recover the approximations of q and ϕ through

$$q \approx q_h := \sum\nolimits_{i=1}^{N} \boldsymbol{q}_i b_i \ ,$$

$$\phi \approx \phi_h := \sum\nolimits_{i=1}^{L} \boldsymbol{\phi}_i b_i + \sum\nolimits_{i=L+1}^{N} u_i b_i \ .$$

Arguments like in the proof of Theorem 1 show that these approximations enjoy the typical quasi-optimality of Galerkin solutions

$$\|q - q_h\|_{\widetilde{H}^{-\frac{1}{2}}(\Sigma)} + \|\phi - \phi_h\|_{H^1(\Sigma)} \leq C \left\{ \inf_{w_h \in V_h} \|q - w_h\|_{\widetilde{H}^{-\frac{1}{2}}(\Sigma)} + \inf_{\nu_h \in V_{h,0}} \|\phi - \nu_h\|_{H^1(\Sigma)} \right\} \ . \quad (20)$$

Here, barring very distorted triangles in $\mathcal{M}_h$, the constant $C > 0$ is independent of the size of the linear system (19). Of course, when the formulation encounters stability problems, *cf.* the discussion in the previous section, then this constant will blow up.

Remark. The computation of the matrix entries of $\boldsymbol{V}$ must be done with high precision, because the distances between two triangles on different connected components of Σ can be very small. Therefore we use accurate semi-analytical integration formulas [2].

Remark. It would also have been possible to approximate q by means of piecewise constant functions on $\mathcal{M}_h$. We opted for basically the same boundary element space for both q and ϕ in order to keep data structures simple.

4.2 Matrix compression

The assembly and solution of the linear system (19) poses two problems:

1. the Galerkin discretization of the integral operator leads to a dense matrix $\boldsymbol{V}$ that requires memory proportional to N^2.

2. the system matrix can be extremely poorly conditioned and the use of a direct solver for the dense system is restricted to problem sizes below 15000 nodes on standard 32-Bit desktop computers.

Only the application of a matrix compression technique like *adaptive cross approximation* (ACA) (Bebendorf 2000, Bebendorf and Rjasanov 2003) for $\boldsymbol{V}$, in combination with an iterative solver can reduce the computational effort, provided a preconditioner can ensure satisfactory convergence. Hence an effective preconditioner has to be constructed. Thereby we take advantage of the compression technique, since the compressed operator is based on so-called *hierarchical matrices* (Grasedyck and Hackbusch 2003, Hackbusch 1999, Hackbusch and Khoromskij 2000). These $\mathcal{H}$-matrices can be employed to perform an approximative Cholesky-decomposition of $\boldsymbol{V}$. Below we will first describe the basic ideas behind ACA and the approximative Cholesky-decomposition by $\mathcal{H}$-matrices. Then we will show, how these techniques are used to construct the preconditioner.

The kernel $1/(4\pi\epsilon_D|\mathbf{x} - \mathbf{x}'|)$ of the single layer boundary integral operator in (15) is smooth, if $\mathbf{x}$ and $\mathbf{x}'$ are well separated. The idea behind all compression techniques is the approximation of the boundary integral operator in the farfield, i.e., in regions where $\mathbf{x}$ and $\mathbf{x}'$ are far away from each other. Well known compression techniques are the fast multipole method (Greengard and Rokhlin 1997), panel clustering (Hackbusch and Nowak 1989), or the $\mathcal{H}^2$-matrix approximation (Börm and Hackbusch 2002). These techniques are based on expansions or interpolations of the kernel-function. An alternative is the so-called *adaptive cross approximation* (ACA) (Bebendorf 2000, Bebendorf and Rjasanov 2003) that is applied here. ACA is a purely algebraic method. It only requires the computation of a small percentage of the entries of the matrix.

---

[2]Thanks to O. Steinbach, G. Of and J. Breuer

8

All compression techniques make use of farfield and nearfield, that have to be defined first. The boundary element basis functions are collected in so-called clusters. Diameter, center, and distance of such clusters can be defined easily. They induce a partitioning of the matrix V into submatrices corresponding to pairs of clusters. A pair of clusters (C_τ, C_σ) and the corresponding submatrix belong to the farfield if the diameters $diam\, C_\tau$, $diam\, C_\sigma$ of the clusters are small compared to their distance $dist\,(C_\tau, C_\sigma)$, i.e. if they fulfill the *admissibility condition*

$$min\{diam\, C_\tau, diam\, C_\sigma\} \leq \eta \cdot dist\,(C_\tau, C_\sigma)\,.$$

The admissibility parameter η is typically chosen between 0.5 and 1.5. If the admissibility condition is not fulfilled, then the submatrix belongs to the nearfield. The submatrices of the nearfield remain uncompressed in all compression techniques. The matrices of the farfield are approximated differently, depending on the specific compression technique.

In the case of ACA one approximates the generically dense submatrices of the farfield by using only a few rows and columns (i.e. crosses) of the submatrix. Other matrix entries, except for these crosses, need not be calculated. One applies this approximation iteratively, starting from only one cross, adding more and more crosses and stopping the sequence of approximations if the difference between two consecutive cross-approximations is small enough. Thus one finds adaptively a *low-rank approximation* of the submatrices of the farfield. Thus ACA compresses the matrix V into a good approximation $\tilde{V}$. Also, matrix-vector multiplication with the compressed matrix becomes much faster. A picture of the resulting ACA-matrix-approximation with the ranks of the submatrices is shown in Figure 4. Full rank submatrices have a dark colour.
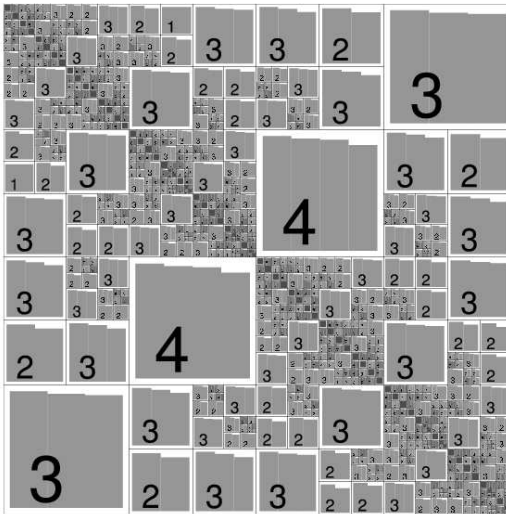

Figure 4: An ACA-matrix-approximation with its rank distribution

The matrices that approximate the boundary integral operator have a special structure for all mentioned compression techniques. They can be regarded as a set of so-called *hierarchical matrices* ($\mathcal{H}$-matrices) (Hackbusch 1999). Arithmetics can be defined on the set of these matrices (Grasedyck and Hackbusch 2003, Hackbusch and Khoromskij 2000) that allow the efficient construction of an approximative Cholesky decomposition $LL^T \approx \tilde{V}$ of the compressed single layer matrix $\tilde{V}$. This decomposition can be used for preconditioning. For further details on the topic we refer to (Bebendorf 2005, Grasedyck and Hackbusch 2003).

4.3   Preconditioned iterative solution

After compression of $\boldsymbol{V}$ with ACA and inserting the approximation $\tilde{\boldsymbol{V}}$ into equation (19) we end up with the equation

$$\boldsymbol{M}\begin{bmatrix} \boldsymbol{q} \\ \boldsymbol{\phi} \end{bmatrix} := \begin{bmatrix} \tilde{\boldsymbol{V}} & \boldsymbol{K} \\ \boldsymbol{K}^T & \boldsymbol{D} \end{bmatrix}\begin{bmatrix} \boldsymbol{q} \\ \boldsymbol{\phi} \end{bmatrix} = \begin{bmatrix} \boldsymbol{\varphi} \\ \boldsymbol{\psi} \end{bmatrix} . \tag{21}$$

We found that all usual preconditioning techniques (Jacobi, ILU, etc.) fail to make an iterative GMRES solver converge. Only the following approach yielded an effective, robust and inexpensive preconditioner:

We start with a matrix factorization

$$\boldsymbol{M} = \boldsymbol{M}_{\tilde{\boldsymbol{V}}} \cdot \boldsymbol{M}_S \ \text{ with } \ \boldsymbol{M}_{\tilde{\boldsymbol{V}}} := \begin{bmatrix} \tilde{\boldsymbol{V}} & 0 \\ 0 & 1 \end{bmatrix}, \ \text{and } \boldsymbol{M}_S := \begin{bmatrix} 1 & \tilde{\boldsymbol{V}}^{-1} \cdot \boldsymbol{K} \\ \boldsymbol{K}^T & \boldsymbol{D} \end{bmatrix} .$$

Next, we make use of the approximative $\mathcal{H}$-Matrix based Cholesky decomposition $\boldsymbol{L} \cdot \boldsymbol{L}^T \approx \tilde{\boldsymbol{V}}$, see Section 4.2 and find

$$\boldsymbol{M}_S \approx \tilde{\boldsymbol{M}}_S := \begin{bmatrix} 1 & (\boldsymbol{L} \cdot \boldsymbol{L}^T)^{-1} \cdot \boldsymbol{K} \\ \boldsymbol{K}^T & \boldsymbol{D} \end{bmatrix} .$$

The preconditioner $\boldsymbol{P}$ is finally defined by

$$\boldsymbol{P} := \tilde{\boldsymbol{M}}_S^{-1} \cdot \boldsymbol{M}_{\tilde{\boldsymbol{V}}}^{-1} \approx \boldsymbol{M}^{-1} .$$

The two "matrix inversions" are realized by another application of preconditioned iterative solvers.

- A good preconditioner for $\boldsymbol{M}_{\tilde{\boldsymbol{V}}}$ can be based on the Cholesky-decomposition $\boldsymbol{L} \cdot \boldsymbol{L}^T \approx \tilde{\boldsymbol{V}}$.

- The matrix $\tilde{\boldsymbol{M}}_S$ can be approximated by using only the diagonal part of $(\boldsymbol{L} \cdot \boldsymbol{L}^T)$. This leads to a sparse matrix for which standard sparse ILU-decompositions (Saad 1995) can be performed that can be used as preconditioners for $\tilde{\boldsymbol{M}}_S$.

5   Results

5.1   Model validation

The model is validated by computing the configuration of Figure 1 for just one turn of radius $R_0 = 9$ cm for a very low frequency of 0.5 Hz. The dimensions are depicted in the caption of Figure 1. The radial distance between the conducting tracks t_D is much smaller then their axial distance d_T and the cylindrical tracks of the capacitor behave in very close approximation to stationary parallel-plate capacitors. The film has a relative dielectric constant of $\epsilon_r = 2.2$. The metallization has a conductivity of $\sigma = 2.5 \cdot 10^6 \frac{1}{\Omega m}$, and is connected to a voltage supply of $U_{\text{peak}} = 1.2$ kV. By using standard formulas for stationary parallel-plate capacitors we expect the surface charge density with values of $q = 1.95 \cdot 10^{-3}$ C/m^2 to be homogeneously distributed over the conducting tracks. This charge is fed by a current density of $j = 6881 \frac{A}{m^2}$ at the contacts. The current density has only axial components.

The results of our computation in Figure 5 are in very good agreement with these estimates. The phase of the current is shifted about $\Pi/2$ compared with the exciting voltage. The imaginary part of the potential, the imaginary part of the surface charge, and the real part of the current density are orders of magnitude smaller than their counterparts of opposite phase. The distance t_D between the conducting tracks is drawn to a larger scale by a factor of 6000 for better visualization in all figures of this section. We used a uniform mesh with 16000 nodes, the computations required
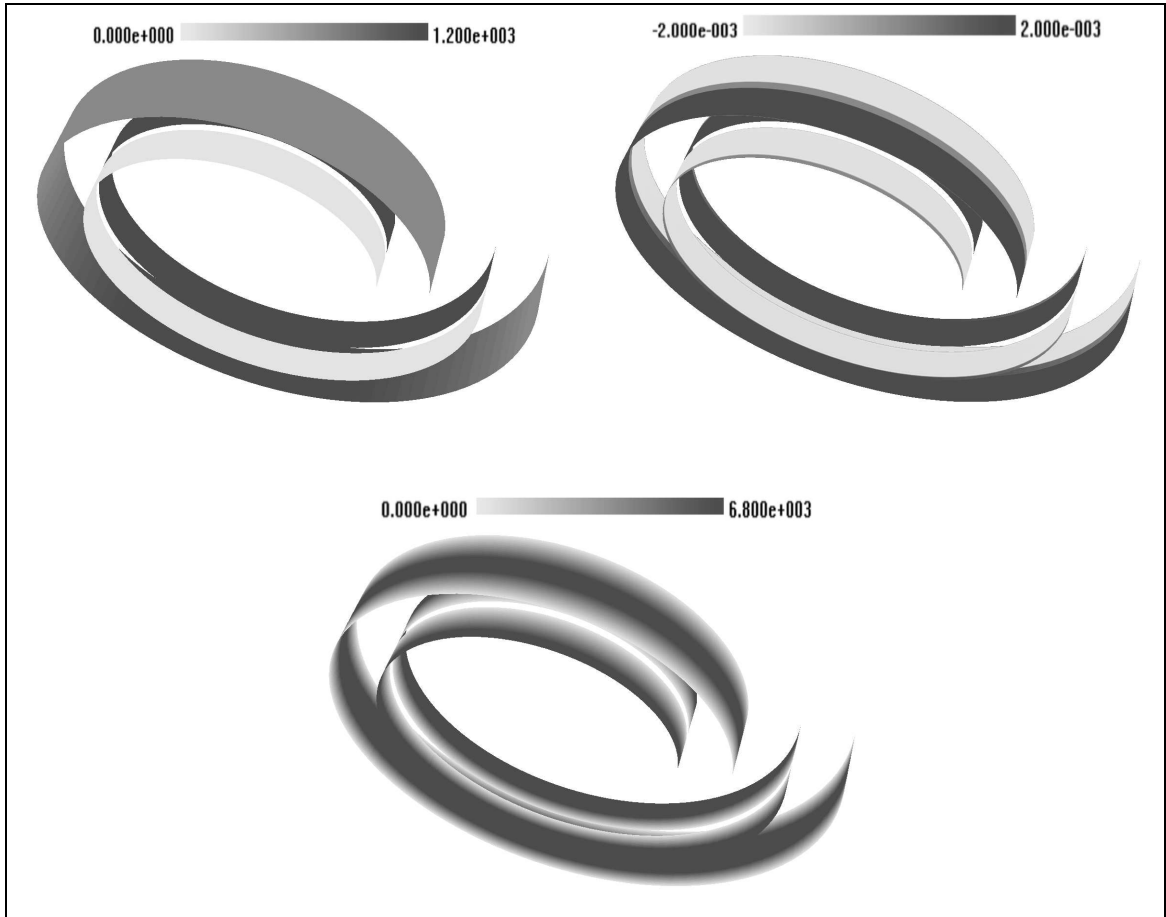
Figure 5: The upper left illustration shows the real part of the potential in $[V]$, the upper right illustration shows the real part of the surface charge density in $[C/m^2]$, and the lower illustration shows the imaginary part of the current density in $[A/m^2]$.
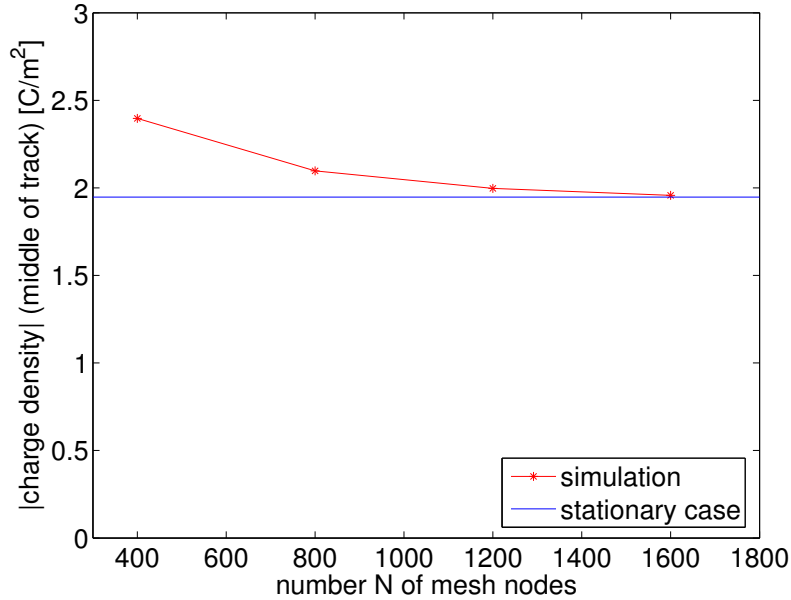
Figure 6: Convergence of simulation results

about 300 MB and the GMRES iterations converged after 23 steps (final relative residual norm 10^{-9}).

We also recorded the computed value of the surface charge density in the middle of the floating track, see Figure 6. The convergence of this value to the charge density in the stationary case (which is a very good approximation in this situation) as finer and finer uniform meshes are used is evident.

5.2   Simulation of Segment Structure

Next we discuss an application of the new simulation method to the practical situation shown in Figure 2. The segment structure of Sheet A is implemented by interrupting the conducting tracks every 130 degrees. This models the situation depicted in Figure 2. All other dimensions and material parameters remained unchanged from the last Section 5.1.

We compare the case of regular service of the capacitor with the defective case. When the capacitor is in regular service, all segments of Sheet A are contacted to the voltage supply. The defective case means that one segment of Sheet A is not connected to the voltage supply. In both cases, even in the defective case, the grounded track of Sheet A is contacted properly. Both cases are simulated for six turns, and the defect is placed in the middle. Figure 7 shows the results of the two computations. The left column is the defective case, and the right column is the regular case.

For the defective case, one easily discerns the non-contacted segment in the central lower part of the spiral by comparing the potentials of the two cases. The floating non-contacted segment of Sheet A is approximately at potential zero. It is covered on each side by a floating part of Sheet B. Each of these adjacent parts is only charged up to half of the normal surface charge density, since it is exposed to the normal electric field from only one side. There is a large additional loss current flowing on Sheet B, with a maximum that is 50% higher than the maximum current on Sheet B for the regular case.

The additional loss current can be understood by looking at Figures 8 and 9. These figures show the uncurled capacitor with Sheet B in the foreground (the edges of the slightly wider Sheet A are visible in the background). Figure 8 shows the surface charge density. The upper illustration shows
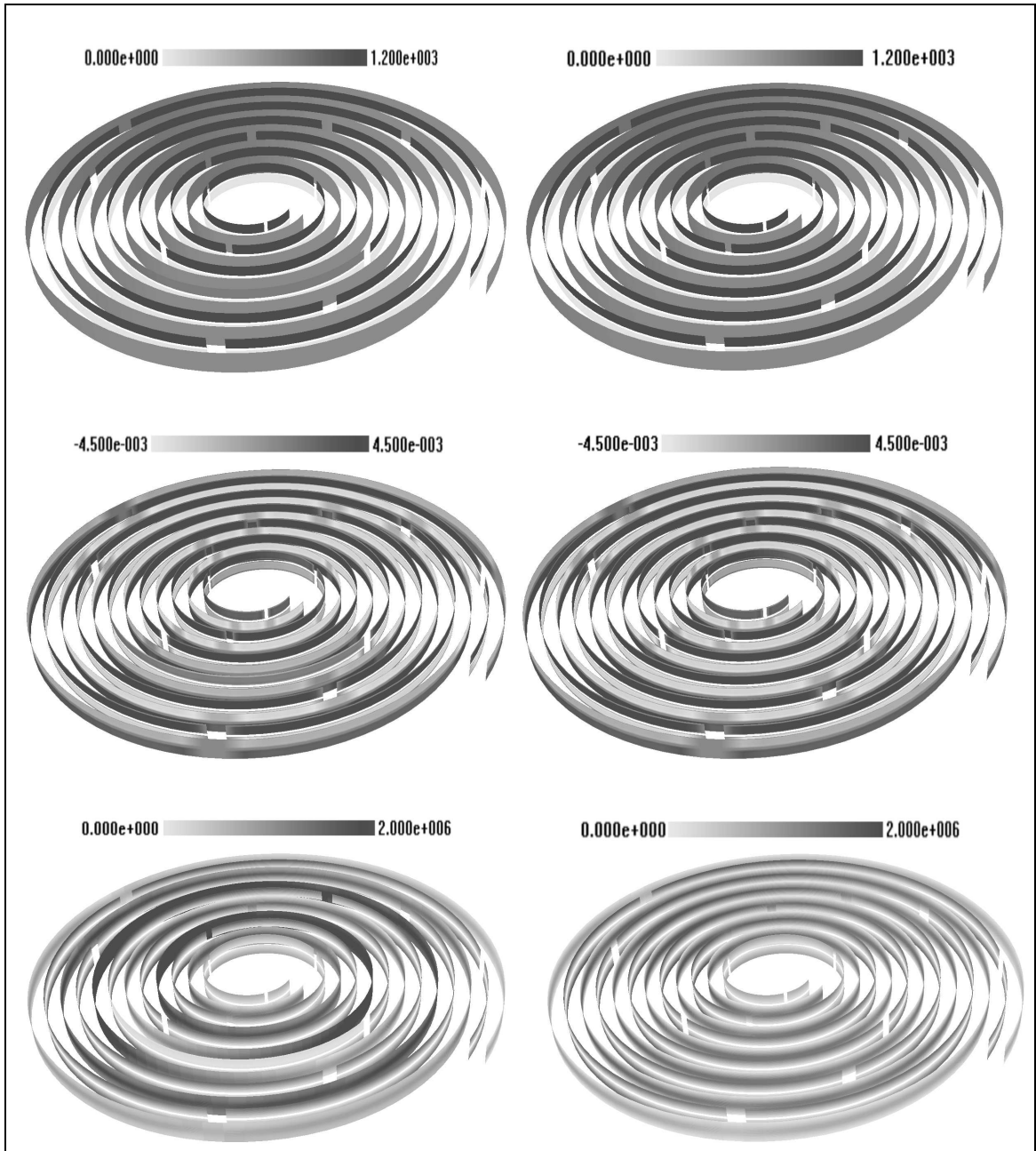
12

Figure 7: The right column shows the results for the regular case; the left column shows the results for the defective case, which includes one non-contacted segment. The first row shows the potentials in $[V]$, the second row shows the surface charge densities in $[C/m^2]$, and the last row shows the current densities in $[A/m^2]$.

the uncurled capacitor in the regular case, whereas the lower illustration shows the defective case. As already mentioned, the two parts of Sheet B that are adjacent to the non-contacted segment of Sheet A carry only half the surface charge density (i.e. approximately $-2.0 \cdot 10^{-3}\,\mathrm{C/m^2}$).
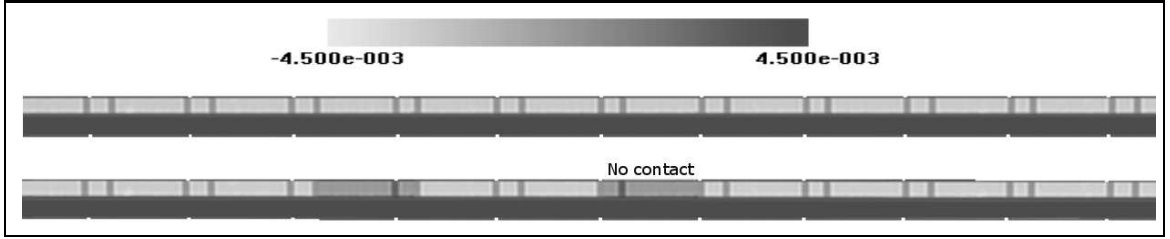

Figure 8: The real part of the surface charge density in $[C/m^2]$ on Sheet B, the floating sheet. The upper illustration shows the surface charge density for the regular case. The lower illustration shows the surface charge density in the defective case.

Figure 9 shows the current densities for the two cases. For the regular case shown in the upper illustration we find a maximum current density of $1.24 \cdot 10^6\,\mathrm{A/m^2}$. The current density has only an axial component, which is in the $\mathbf{e}_z$-direction. The current density in the lower illustration shows the defective case with a maximum of $2.0 \cdot 10^6\,\mathrm{A/m^2}$. It has components in the axial $\mathbf{e}_z$-direction as well as in the $\mathbf{e}_\varphi$-direction. This can be explained by taking a look at the surface charge of Figure 8 for the defective case. The surface charge is asymmetrically distributed on Sheet B. This asymmetry results from the fact that all segments of the grounded track of Sheet A are contacted to earth, whereas there is a non-contacted segment on the other track of Sheet A. This means that the surface charge density of Sheet B must be fed from a non-axial current in $\mathbf{e}_\varphi$ direction.
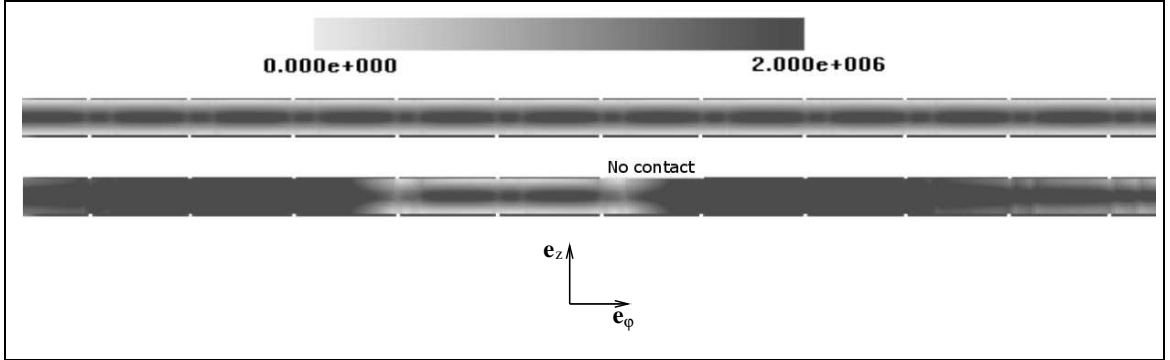

Figure 9: The imaginary part of the current density in $[A/m^2]$ on Sheet B, the floating sheet. The upper illustration shows the current density for the regular case, containing only a $\mathbf{e}_z$ component. The lower illustration shows the current density in the defective case. Its maximum is 50% higher than the maximum for the regular case, and the additional loss current goes in the $\mathbf{e}_\varphi$ direction.

We found the preconditioner $\boldsymbol{P}$ and ACA to work well within the applied GMRES for the two computations. We used the same grid for both defective and regular cases, and the GMRES converged to a final relative residual norm of approximately 10^{-9} in less then 50 steps. The grid consists of 38000 nodes, i.e. approximately 76000 complex unknowns, and the solver required in total approximately 700 Megabytes of memory for the solution.

Acknowledgment

References

M. Bebendorf (2000), 'Approximation of boundary element matrices', *Numer. Math.* **86**(4), 565–589.

M. Bebendorf (2005), 'Hierarchical *LU* decomposition-based preconditioners for BEM', *Computing* **74**, 225–247.

M. Bebendorf and S. Rjasanov (2003), 'Adaptive low-rank approximation of collocation matrices', *Computing* **70**, 1–24.

M. Berqvist, C. Törnkvist and J. Mood (2004), 'Dryq - a dry insulated, high voltage power capacitor', *IEEE/PES T&D Conference Sao Paulo*.

S. Börm and W. Hackbusch (2002), '$\mathcal{H}^2$-matrix approximation of integral operators by interpolation', *Applied Numerical Mathematics* **43**, 129–143.

F. Brezzi and M. Fortin (1991), *Mixed and hybrid finite element methods*, Springer.

M. W. Carlen and P. Brüesch (1996), 'Electrical endurance characterization of polypropylene winding capacitors for traction applications: a new experimental method', *Seventh Int. Conference on Dielectric Materials Measurements and Applications, Publication No.430* pp. 350–353.

C. Charlton (1955), 'Self-healing in metallized paper capacitors', *TMC Tech. Jour.* **6**, 27–41.

T. Christen and M. Carlen (2003), 'Recent progress in the physics of capacitors', *Recent Res. Devel. Applied Phys.* **6**, 517–545.

M. Costabel (1987), Symmetric methods for the coupling of finite elements and boundary elements, in *Boundary Elements IX* (C. Brebbia, W. Wendland and G. Kuhn, eds), Springer-Verlag, Berlin, pp. 411–420.

H. Dirks (1996), 'Quasi–stationary fields for microelectronic applications', *Electrical Engineering* **79**, 145–155.

B. Drugge, M. Carlen, S. Laihonen and L. Spronck (2003), 'Cut and dried! A new dry capacitor for high voltage DC applications', *ABB Review* **1**, 15–20.

L. Grasedyck and W. Hackbusch (2003), 'Construction and arithmetics of $\mathcal{H}$-matrices', *Computing* **70**, 295–334.

L. Greengard and V. Rokhlin (1997), 'A new version of the fast multipole method for the Laplace equation in three dimensions', *Acta Numerica* pp. 229–269.

W. Hackbusch (1999), 'A sparse matrix arithmetic based on $\mathcal{H}$-matrices. Part I: Introduction to $\mathcal{H}$-matrices', *Computing* **62**, 89–108.

W. Hackbusch and B. Khoromskij (2000), 'A sparse $\mathcal{H}$-matrix arithmetic. Part II: Application to multidimensional problems', *Computing* **64**, 21–47.

W. Hackbusch and Z. Nowak (1989), 'On the fast matrix multiplication in the boundary element method by panel clustering', *Numer. Math.* **54**, 463–491.

H. Heywang (1976), 'Physikalische und chemische Vorgänge in selbstheilenden Kunststoff-Kondensatoren', *Colloid and Polymer Sci.* **254**, 139–147.

C. Johnson and J. Nédélec (1980), 'On the coupling of boundary integral and finite element methods', *Math. Comp.*

J. Kammermaier (1964), 'Untersuchung der Umsetzungsprozesse bei Durchschlägen in Kondensatoren mit metallisiertem Dielektrikum', *Schwachstromtechnik* **18**(5), 145–150.

J. Kammermaier, G. Rittmayer and S. Birkle (1989), 'Modeling of plasma-induced self-healing in organic dieletrics', *J. Appl. Phys.* **66**(4), 1594–1609.

J.-F. Kiang (1996), 'Quasistatic analysis of microstrip lines on lossy inhomogeneous substrates', *IEE Proc. Microwaves, Antennas and Propagation* **143**(5), 1350–2417.

A. Kohler (1956), 'Le condensateur au papier métallisé', *L'onde électrique* **36**, 842–851.

C. Reed and S. Cichanowski (1994), 'The fundamentals of aging in hv polymer-film capacitors', *IEEE Trans. Dielectrics and Electrical Insulation* **1**(5), 904–922.

S. Reitzinger, U. Schreiber and U. van Rienen (2003), 'Electro-quasistatic calculation of electric field strength on high-voltage insulators with an algebraic multigrid algorithm', *IEEE Trans. Magnetics* **39**(4), 2129–2132.

Y. Saad (1995), *Iterative methods for sparse linear systems*, PWS Publishing Co.

S. Sauter and C. Schwab (2004), *Randelementmethoden*, BG Teubner, Stuttgart.

H. Sträb (1954), *Die Selbstheilung von MP-Kondensatoren und ihre Auswirkungen im Dauerlauf*, number 18 *in* 'VDE Berichte', VDE.